

Active Magneto-Optical Control of Near-Field Radiative Heat Transfer between Graphene Sheets

Huihai Wu,¹ Yong Huang,^{1,*} Longji Cui,^{2,3} and Keyong Zhu¹

¹*School of Aeronautic Science and Engineering, Beihang University, Beijing 100191, China*

²*The Smalley-Curl Institute, Rice University, Houston, Texas 77005, USA*

³*Department of Physics and Astronomy, Rice University, Houston, Texas 77005, USA*



(Received 14 February 2019; revised manuscript received 11 April 2019; published 8 May 2019)

In this paper, we investigate active control of near-field radiative heat transfer between monolayer graphene sheets by a magnetic field. We predict the existence of the giant thermal magnetoresistance (e.g., approximately 2.0 for $B = 1$ T and 50.0 for $B = 20$ T) and negative thermal magnetoresistance of near-field radiative heat flux for different Fermi energies. Moreover, we observe Shubnikov–de Haas-like oscillations in the spectral heat flux, originating from the intraband or interband transitions between various Landau levels. Our findings provide alternative insights into the active control of near-field thermal radiation and may be leveraged for potential applications in noncontact thermal management.

DOI: [10.1103/PhysRevApplied.11.054020](https://doi.org/10.1103/PhysRevApplied.11.054020)

I. INTRODUCTION

The radiative heat transfer between two bodies separated by a vacuum gap smaller than the thermal wavelength (i.e., in the near field, approximately $10\ \mu\text{m}$ at room temperature) can exceed Planck's black-body limit by several orders of magnitude due to evanescent wave tunneling, especially when the materials support surface resonance modes [1–3]. Near-field radiative heat transfer (NFRHT) has potential applications in many areas, such as thermophotovoltaics [4–7], thermal imaging [8], heat-assisted magnetic recording [9], radiative cooling [10–12], and thermal management [13–15]. The issue of the active control of NFRHT has received considerable critical attention.

Graphene provides an ideal platform for active modulation of NFRHT, due to its large tunability and strong optical response in the infrared and terahertz regions [16, 17]. The near-field thermal radiation of graphene and its applications has been widely studied in a variety of configurations such as suspended graphene sheets [18, 19], graphene nanostructures [20–22], and graphene covered substrates [23–29]. However, much of the research on the modulation of NFRHT in graphene is based on tuning the chemical potential by doping or by gating.

Here, we propose a new scheme of noncontact active modulation of the NFRHT between two monolayer graphene sheets by external static magnetic fields. There have been some studies on the effects of magnetic fields on the near-field thermal radiation [30] and near-field thermomagnetic effect, such as the persistent directional

heat current [31], near-field thermal Hall effect [32], giant thermal magnetoresistance [33], and anisotropic thermal magnetoresistance [34]. However, most studies have been restricted to conventional magneto-optical semiconductors, like InSb. The authors of such studies have focused on the semiclassical regime and ignored Landau quantization. Graphene provides unusual magneto-optical properties when an external magnetic field is applied perpendicularly, such as quantum Faraday effects and Kerr effects [35–37], due to it having nonequidistant quantized Landau levels [38, 39], which are dependent on the square root of B , given by $E_n = \text{sign}(n)(\hbar v_F/l_B)\sqrt{2|n|}$, where $v_F \approx 10^6$ m/s denotes the Fermi velocity of carriers; $l_B = \sqrt{\hbar/eB}$ is the magnetic length; and $n = 0, \pm 1, \pm 2, \dots$ is the Landau level index. In contrast, Landau levels of conventional two-dimensional electron systems (2DES) are equally spaced. The hybridization between plasmons and cyclotron excitations results in the formation of magneto-plasmon polariton (MPP) modes in graphene [40–42], which greatly enhances light-matter interactions.

In this paper, we show that in the presence of a static magnetic field, the coupling of the excited MPP modes of graphene in the near field greatly enhances the radiative heat transfer, exceeding the black-body limit by several orders of magnitude. Because of the intraband and interband transitions between various Landau levels, the dispersion curves of the MPP mode split into many branches with respect to the zero-field surface plasmon (SP) mode, resulting in a series of peaks in the near-field radiative spectral heat flux and Shubnikov–de Haas-like oscillations around the zero-field spectrum. Moreover, we demonstrate

*huangy@buaa.edu.cn

that a magnetic field can strongly modulate the NFRHT of graphene, in conjunction with the different Fermi energies tuned by doping or gating. For example, at room temperature, the near-field heat flux of graphene at low Fermi energies is significantly inhibited by the magnetic field, exhibiting giant thermal magnetoresistances, while for high Fermi energies the heat flux is weakly affected, showing negative thermal magnetoresistance, which is a thermal analogy of the negative magnetoresistance for some materials (such as topological materials [43]) in electronics.

II. NEAR-FIELD RADIATIVE HEAT TRANSFER

The net radiative heat exchange between two graphene sheets can be derived in the framework of the fluctuation-dissipation theorem and dyadic Green function, given by

$$\mathbf{T}(\omega, k; d) = \begin{cases} \text{Tr}[(\mathbf{I} - \mathbf{R}_2^\dagger \mathbf{R}_2 - \mathbf{T}_2^\dagger \mathbf{T}_2) \mathbf{D}_{12} (\mathbf{I} - \mathbf{R}_1 \mathbf{R}_1^\dagger - \mathbf{T}_1 \mathbf{T}_1^\dagger) \mathbf{D}_{12}^\dagger], & k < k_0, \\ \text{Tr}[(\mathbf{R}_2^\dagger - \mathbf{R}_2) \mathbf{D}_{12} (\mathbf{R}_1 - \mathbf{R}_1^\dagger) \mathbf{D}_{12}^\dagger] e^{-2|k_{z0}d}, & k > k_0. \end{cases} \quad (3)$$

Here, $k_0 = \omega/c$ is the wave vector in vacuum, $k_{z0} = \sqrt{k_0^2 - k^2}$ is the wave-vector component perpendicular to the interface, and $k = \sqrt{k_x^2 + k_y^2}$ is the transverse wave vector parallel to the interface. $\mathbf{D}_{12} = (\mathbf{I} - \mathbf{R}_1 \mathbf{R}_2 e^{2ik_{z0}d})^{-1}$ denotes the Fabry-Perot-like denominator matrix and \mathbf{R}_i is the reflection coefficient matrix given by

$$\mathbf{R}_i = \begin{bmatrix} r_i^{ss} & r_i^{sp} \\ r_i^{ps} & r_i^{pp} \end{bmatrix}. \quad (4)$$

Here, r_i^{mn} ($i = 1, 2$) is the Fresnel reflection coefficient of the i th body. m and n represent the polarization states (p or s polarization) of incident waves and reflection waves, respectively.

For a general two-dimensional material, its optical conductivity is a tensor, given by

$$\bar{\bar{\sigma}}(\omega, \mathbf{q}) = \begin{bmatrix} \sigma_{xx}(\omega, \mathbf{q}) & \sigma_{xy}(\omega, \mathbf{q}) \\ \sigma_{yx}(\omega, \mathbf{q}) & \sigma_{yy}(\omega, \mathbf{q}) \end{bmatrix}, \quad (5)$$

where angular frequency ω and wave vector \mathbf{q} represent temporal and spatial dispersion, respectively. If the non-local effect is not considered, then $\mathbf{q} \rightarrow 0$. The reflection coefficients of graphene covered on an isotropic substrate

the Landauer-like formalism [30]

$$\begin{aligned} q(T_1, T_2; d) &= \int_0^\infty \frac{d\omega}{2\pi} q(\omega) \\ &= \int_0^\infty \frac{d\omega}{2\pi} [\Theta(\omega, T_2) - \Theta(\omega, T_1)] \Phi(\omega). \end{aligned} \quad (1)$$

Here, $q(\omega)$ is the spectral radiative heat flux, $\Theta(\omega, T) = \hbar\omega / [\exp(\hbar\omega/k_B T) - 1]$ is the mean energy of the Planck oscillator, and $\Phi(\omega)$ is the spectral energy transfer function given by

$$\Phi(\omega) = \int_0^\infty \frac{kdk}{4\pi^2} \mathbf{T}(\omega, k; d), \quad (2)$$

where $\mathbf{T}(\omega, k; d)$ is the energy transmission coefficient, given by [44,45]

are given by

$$\begin{aligned} r_{ss} &= \frac{(\xi_a + 1)(1 - \xi_c) + \xi_b \xi_d}{(\xi_a + 1)(\xi_c + 1) - \xi_b \xi_d}, \\ r_{sp} &= \frac{2\xi_b}{(\xi_a + 1)(\xi_c + 1) - \xi_b \xi_d}, \\ r_{ps} &= \frac{-2\xi_d}{(\xi_a + 1)(\xi_c + 1) - \xi_b \xi_d}, \\ r_{pp} &= \frac{(\xi_a - 1)(\xi_c + 1) - \xi_b \xi_d}{(\xi_a + 1)(\xi_c + 1) - \xi_b \xi_d}. \end{aligned} \quad (6)$$

Here, we introduce four parameters: $\xi_a = (\sigma_{xx}/(\omega\varepsilon_0) + \varepsilon/q)k_z$, $\xi_b = \sqrt{\mu_0/\varepsilon_0}\sigma_{xy}$, $\xi_c = (\sigma_{yy}\omega\mu_0 + q)/k_z$, and $\xi_d = \sqrt{\mu_0/\varepsilon_0}\sigma_{yx}$. ε_0 and μ_0 are permittivity and permeability, respectively. ε and μ are relative permittivity and permeability of the substrate, respectively. $q = \sqrt{\varepsilon\mu(\omega/c)^2 - k^2}$ are perpendicular wave vectors in the substrate, and k_z and k are perpendicular and parallel wave vectors in vacuum, respectively. In this paper, we focus on the suspended graphene, and ε and μ are set to 1.0. The reflection coefficients are simplified as

$$\begin{aligned} r_{ss} &= -[2Z_0\sigma_L/\lambda + Z_0^2(\sigma_L^2 + \sigma_H^2)]/D, \\ r_{sp} &= r_{ps} = 2Z_0\sigma_H/D, \\ r_{pp} &= [2Z_0\lambda\sigma_L + Z_0^2(\sigma_L^2 + \sigma_H^2)]/D. \end{aligned} \quad (7)$$

Here, Z_0 is the impedance of free space, $k_0 = \omega/c$ is the wave vector in vacuum, $\lambda = k_z/k_0$, and $D = 4 + 2Z_0(1/\lambda + \lambda)\sigma_L + Z_0^2(\sigma_L^2 + \sigma_H^2)$.

III. OPTICAL CONDUCTIVITY

The optical conductivity of zero-field graphene is a scalar, given by

$$\sigma = \sigma_D + \sigma_I. \quad (8)$$

Here, σ_D and σ_I are the Drude (intraband) contribution and interband contribution, respectively, given by [46]

$$\sigma_D = \frac{i}{\omega + i/\tau} \frac{e^2 2k_B T}{\pi \hbar^2} \ln \left(2 \cosh \frac{\mu}{2k_B T} \right), \quad (9)$$

$$\sigma_I = \frac{e^2}{4\hbar} \left[G \left(\frac{\hbar\omega}{2} \right) + i \frac{4\hbar\omega}{\pi} \int_0^\infty \frac{G(x) - G(\hbar\omega/2)}{(\hbar\omega)^2 - 4x^2} dx \right], \quad (10)$$

where $G(x) = \sinh(x/k_B T) / [\cosh(\mu/k_B T) + \cosh(x/k_B T)]$ and μ is the chemical potential.

When a vertical static magnetic field is applied, the conductivity of graphene becomes a tensor with nonzero diagonal and nondiagonal elements. In this paper, we neglect spatial dispersion ($\mathbf{q} \rightarrow 0$); thus, $\sigma_{xx} = \sigma_{yy} = \sigma_L(\omega)$ and $\sigma_{xy} = -\sigma_{yx} = \sigma_H(\omega)$, where $\sigma_{L(H)}$ is the longitudinal (Hall) conductivity. For the strong magnetic field or low electron density, the response of electrons to an external magnetic field is characterized in the quantum regime and the magneto-optical conductivity can be written as [47,48]

$$\begin{aligned} \sigma_{L(H)}(\omega, B) \\ = g_s g_v \times \frac{e^2}{4\hbar} \sum_{n \neq m = -N_C}^{N_C} \frac{\Lambda_{L(H)}^{nm}}{iE_{nm}} \frac{n_F(E_n) - n_F(E_m)}{\hbar\omega + E_{nm} + i\Gamma_{nm}(\omega)}. \end{aligned} \quad (11)$$

Here, $g_{s(v)} = 2$ is the spin (valley) degeneracy factor of graphene and $n_F(E) = 1/[1 + e^{(E-E_F)/k_B T}]$ is the Fermi-Dirac distribution, where E_F is the Fermi energy. $E_n = \text{sign}(n)(\hbar v_F/l_B)\sqrt{2|n|}$ are the Landau energy levels, where $l_B = \sqrt{\hbar/eB}$ is the magnetic length and $n = 0, \pm 1, \pm 2, \dots$ is the Landau level index. $v_F \approx 10^6$ m/s denotes the Fermi velocity of carriers in graphene. Obviously, the Landau level spacing is nonequidistant. $\Gamma_{nm}(\omega)$ is the Landau level broadening, taken as 6.8 meV [47]. $E_{nm} = E_n - E_m$ and

$$\begin{aligned} \Lambda_L^{nm} &= \frac{\hbar^2 v_F^2}{l_B^2} (1 + \delta_{n,0} + \delta_{m,0}) \delta_{|n|-|m|, \pm 1}, \\ \Lambda_H^{nm} &= i \Lambda_L^{nm} (\delta_{|n|-1, |m|} - \delta_{|n|, |m|-1}). \end{aligned} \quad (12)$$

Here, $|n|, |m| \leq N_C$ with $N_C = \text{int}[(E_{\text{cut}}/E_1)^2]$ and the cut-off energy $E_{\text{cut}} = 3.0$ eV [42]. Equation (11) contains the

intraband ($n = m \pm 1$) and interband ($n = -m \pm 1$) transitions.

In Fig. 1, we plot the real (solid curves) and imaginary (dashed curves) parts of the longitudinal magneto-optical conductivity of graphene as a function of frequency for $T = 300$ K and $B = 5$ T. The red and blue curves represent $E_F = 0.05$ eV and $E_F = 0.2$ eV, respectively. For $E_F = 0.05$ eV, we have $E_F < E_1 \approx 0.08$ eV, graphene has a relatively low electron density and high Landau level, the intraband transitions are partially blocked, and the interband transitions play a dominant role, which gives rise to a series of absorption peaks (maxima of the real part) at $\hbar\omega_{\text{peak}}^{\text{inter}} \approx E_{n+1} + E_n$ ($n = 0, 1, \dots$) and the Shubnikov-de Haas (SDH) oscillations of the conductivity around the universal conductivity $\sigma_0 = e^2/4\hbar$ for the real part and 0 for imaginary part at high frequencies. The weak peak at $\hbar\omega \approx E_2 - E_1$ originates from the intraband transition due to the thermal effect.

For the case of higher electron density ($|E_F| = 0.2$ eV $> E_1$), some low-frequency interband transitions are blocked and intraband transitions dominate, resulting in one strong absorption peak at $\hbar\omega_{\text{peak}}^{\text{intra}} \approx (\sqrt{N_F + 1} - \sqrt{N_F}) E_1$, where $N_F = \text{int}[(E_F/E_1)^2]$ is the last occupied Landau level. For the photon energy above the transition threshold $\hbar\omega = (\sqrt{N_F} + \sqrt{N_F + 1}) E_1$, interband transitions begin to play a role, leading to a series of peaks as $\hbar\omega_{\text{peak}}^{\text{inter}} = E_{n+1} + E_n = (\sqrt{n+1} + \sqrt{n}) E_1$, where $n \geq N_F$. In fact, the temperature effect broadens the frequency range of the interband contribution, which can also play a role even below the transition threshold.

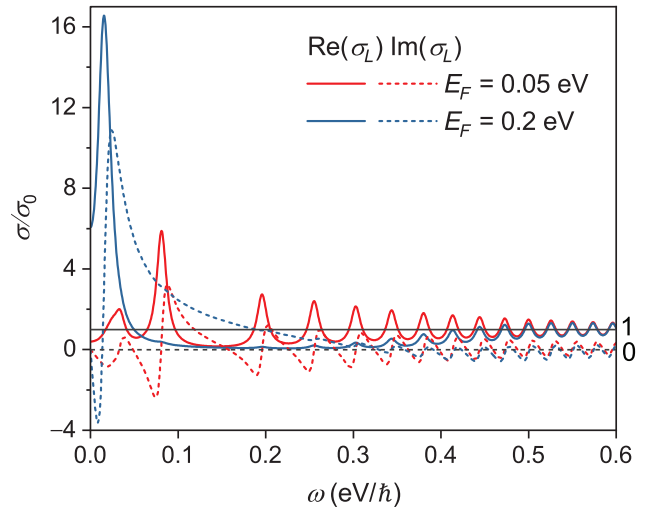


FIG. 1. Longitudinal magneto-optical conductivity of graphene in a quantum regime divided by the universal conductivity $\sigma_0 = e^2/4\hbar$, for $B = 5$ T and $T = 300$ K. The red and blue curves denote Fermi energies of $E_F = 0.05$ eV and $E_F = 0.2$ eV, respectively. The solid and dashed curves represent the real and imaginary parts of the conductivity, respectively.

IV. RESULTS AND DISCUSSION

A. Near-field radiative heat flux

We consider two suspended monolayer graphene sheets in vacuum separated by a gap of d as shown in Fig. 2(a). We focus on the radiative heat transfer coefficient (RHTC), which can be expressed as

$$h(T, d, B) = \lim_{\Delta T \rightarrow 0} \frac{q(T_1=T, T_2=T+\Delta T; d)}{\Delta T} = \int_0^\infty d\omega \frac{\partial}{\partial T} \Theta(\omega, T) \int_0^\infty \frac{kdk}{4\pi^2} \mathbf{T}(\omega, k; d). \quad (13)$$

The thermal magnetoresistance is given by $R(B) = 1/h(B)$ and the relative thermal magnetoresistance ratio (TMR) can be defined as

$$\text{TMR} = \frac{R(B) - R(0)}{R(0)} = \frac{h(0)}{h(B)} - 1. \quad (14)$$

When $h(B) > h(0)$, TMR is negative.

In Fig. 2, we calculate the RHTC and the ratio of zero-field RHTC to nonzero-field RHTC between two graphene sheets as a function of the gap size for different magnetic fields. We consider two cases: low electron density with $E_F = 0.05$ eV $< E_1$ and high electron density with $E_F = 0.5$ eV $> E_1$, represented by the solid and dashed curves, respectively. The curves with different colors represent different magnetic fields. The results show that, in the near field, the RHTC of graphene in different magnetic fields, both for a high and low Fermi energy, can be several orders of magnitude higher than that of the black body.

For the lower Fermi energy of $E_F = 0.05$ eV, the near-field RHTC of graphene is strongly suppressed by the magnetic field and the reduction rate of heat flux increases with the magnetic field, leading to a giant thermal magnetoresistance, with no saturation behavior with the increase of magnetic field. For example, the reduction rate can

exceed 1 order of magnitude for $B = 20$ T for the gap size of approximately 1–100 nm, and thus, $h(0)/h(B)$ can be as high as 10.0, as shown in Fig. 2(c), and will continue to increase with the magnetic field (not shown), which is different from the saturation behavior in bulk magneto-optical materials [30]. Moreover, the heat fluxes at different gap sizes have different responses to the magnetic field and $h(0)/h(B)$ exhibits a nonmonotonic dependence on the gap size. For $d < 100$ nm, because RHTC in the magnetic field has a similar distance-scaling law to that in zero field, $h(0)/h(B)$ varies slightly with d . As the gap size increases, RHTC has a faster rate of decline for a stronger magnetic field, leading to a higher peak of $h(0)/h(B)$ [e.g., $h(0)/h(B) \approx 2.0$ for $B = 1$ T at approximately $4 \mu\text{m}$ and $h(0)/h(B) \approx 48.0$ for $B = 20$ T at approximately $0.7 \mu\text{m}$] and a giant thermal magnetoresistance. In the far field, the contributions of evanescent waves fade away, propagating waves dominate, and the RHTC asymptotically converges to a constant value, which increases with the magnetic field. Therefore, as shown in Fig. 2(c), $h(0)/h(B)$ is independent of d in the far field and less than 1.0, resulting in a negative TMR, which is a thermal analog of the negative magnetoresistance in electronics. The minimum value of TMR is about -90% at $B = 15$ T and the corresponding RHTC is about an order of magnitude higher than the zero-field value.

Compared with the above case of $E_F = 0.05$ eV, for a high Fermi energy $E_F = 0.5$ eV, the effect of the magnetic field on the near-field RHTC of graphene is much weaker, even for a very strong magnetic field. As shown by the dashed curves in Fig. 2(b), the different curves nearly coincide with each other in the near field, whereas in the far field, the magnetic field greatly enhances the RHTC, similar to the case of $E_F = 0.05$ eV. As shown in Fig. 2(d), when the gap size is smaller than $1 \mu\text{m}$, the magnetic field can slightly enhance RHTC, leading to $h(0)/h(B) < 1$ and

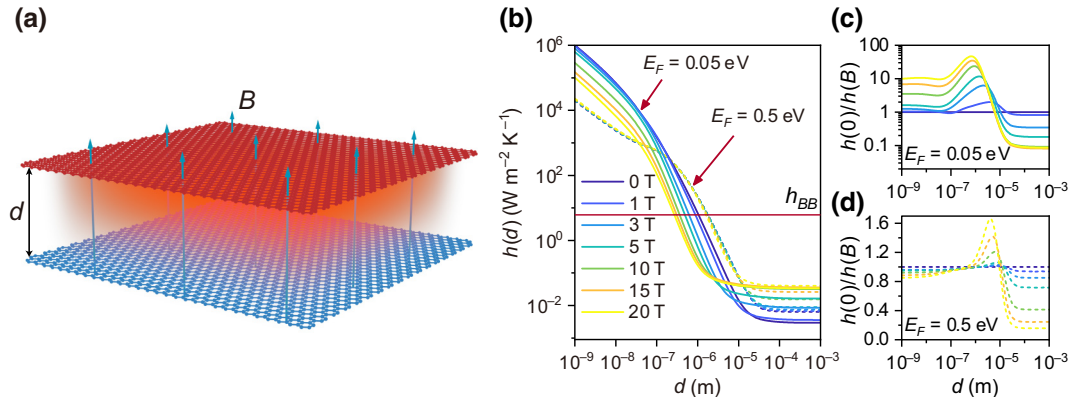


FIG. 2. (a) Schematic of near-field radiative heat transfer between two monolayer graphene sheets in the presence of a magnetic field perpendicular to the plane. (b) RHTC between two graphene sheets as a function of the gap size. (c),(d) The ratio of RHTC in zero field to that in the presence of magnetic fields. The temperature of graphene is 300 K. The solid and dashed curves denote the Fermi energies of $E_F = 0.05$ eV and $E_F = 0.5$ eV, respectively. The red solid line in (b) is the RHTC of the black body given by $h_{\text{BB}} = 4\sigma_{\text{SB}}T^3 \approx 6.1 \text{ W m}^{-2} \text{ K}^{-1}$, where σ_{SB} is the Stefan-Boltzmann constant.

a negative TMR ($\text{TMR} \geq -20\%$). For a separation from 1 to 10 μm , we have $h(0)/h(B) \geq 1$ and a small peak with a value of 1.6, and heat flux in this region is suppressed. For the separation of $d > 10 \mu\text{m}$, RHTC gradually converges, $h(0)/h(B) < 1$, and TMR is also negative, with a maximum of -85% .

The difference between RHTC at a lower Fermi energy and higher Fermi energy also depends on the gap size and magnetic field. At a small gap size ($< 100 \text{ nm}$), the heat flux for $E_F = 0.5 \text{ eV}$ is much lower than that for $E_F = 0.05 \text{ eV}$, but the difference between the two cases decreases with the magnetic field. In contrast, at the gap size of $100 \text{ nm} < d < 10 \mu\text{m}$, due to the small decline rate, the heat flux for $E_F = 0.5 \text{ eV}$ gradually exceeds the value for $E_F = 0.05 \text{ eV}$, and the difference between two cases increases with the magnetic field. In the far field, the heat flux for the two cases tends to be consistent in a strong magnetic field.

B. Near-field spectral radiative heat transfer

Now, we turn to the near-field radiative spectral heat flux. In Fig. 3, we calculate the energy transfer function $\Phi(\omega)$ and spectral RHTC $h(\omega)$, given by

$$h(\omega) = \partial/\partial T[\Theta(\omega, T)]\Phi(\omega) \quad (15)$$

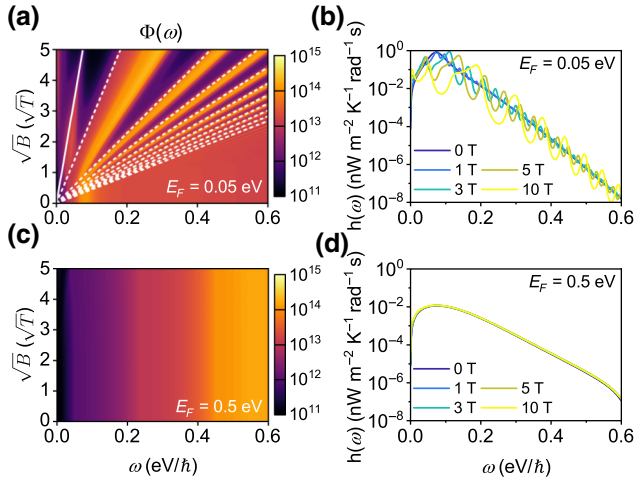


FIG. 3. (a),(c) Contour plots of energy transfer function $\Phi(\omega)$ as a function of angular frequency and square root of B for $E_F = 0.05 \text{ eV}$ and $E_F = 0.5 \text{ eV}$. The white lines in (a) denote linear dependence of the transition energy on the square root of magnetic field: the solid line is the intraband transition $E_1 \rightarrow E_2$ with energy gap $\hbar\omega = (\sqrt{2} - 1)E_1$, and the dashed lines denote the interband transitions of Landau levels $E_{-n} \rightarrow E_{n+1}$ and $E_{-(n+1)} \rightarrow E_n$ with energy gaps $\hbar\omega = (\sqrt{n+1} + \sqrt{n})E_1$. (b),(d) Spectral RHTC $h(\omega)$ in different magnetic fields for $E_F = 0.05 \text{ eV}$ and $E_F = 0.5 \text{ eV}$, respectively. The temperatures of graphene sheets are at 300 K. The gap size is 10 nm.

in different magnetic fields for $E_F = 0.05 \text{ eV}$ and $E_F = 0.5 \text{ eV}$, respectively. Considering that the peak frequencies of the magneto-optical conductivity are proportional to the first Landau level $E_1 = \sqrt{2}v_F^2\hbar/e\sqrt{B}$, in Figs. 3(a) and 3(c), we plot the contours of $\Phi(\omega)$ as a function of ω and \sqrt{B} .

The results suggest that in a low magnetic field ($E_1 < E_F$), there is no significant change in $\Phi(\omega)$ compared with that in zero field for the case of $E_F = 0.05 \text{ eV}$, and a broadband peak appears in $\Phi(\omega)$ at low frequencies and flattens at high frequencies due to the intraband contribution. For the higher magnetic field ($E_1 > E_F$), the low-field peak splits into several peaks, resulting in alternating bright and dark radial stripes like moiré patterns, distributed in the high-frequency region. The bright stripes show a linear dependence of the frequencies on \sqrt{B} as $\hbar\omega_{\text{peak}} \propto \sqrt{B}$ and have a one-to-one correspondence with the interband transition lines $\hbar\omega_{\text{peak}}^{\text{inter}} = (\sqrt{n+1} + \sqrt{n})E_1$, as shown in Fig. 3(a), but they are not completely coincident with each other, especially for a smaller n . Meanwhile, the period and contrast of the bright and dark stripes increase with magnetic field, but decrease with frequency. Therefore, in the frequency region of $\hbar\omega > 0.1 \text{ eV}$ in Fig. 3(b), $\Phi(\omega)$ oscillates around the zero-field spectrum, giving rise to a series of peaks whose values and spacing decrease with frequency. The amplitude of oscillation increases with the magnetic field but those peaks become sparse and broadband, and their frequencies are blueshifted with the magnetic field. Those manifestations are similar to SDH oscillations of the conductivity [47], so we call them SDH-like oscillations. In addition, we observe two bright stripes at low frequencies in Fig. 3(a) corresponding to two low-frequency peaks in Fig. 3(b), one near the intraband transition with energy difference $\hbar\omega = (\sqrt{2} - 1)E_1$ [solid line in Fig. 3(a)], whose frequency is proportional to \sqrt{B} and whose value first increases but then significantly decreases with the magnetic field, having a maximum value of $\Phi(\omega) \approx 4.5 \times 10^{13} \text{ m}^{-2}$ at $B \approx 4 \text{ T}$, and the other at near-zero frequency, whose value increases with the magnetic field. These two stripes have smaller values than those of others, but play an important role in the whole heat flux due to the exponential decay of $\partial/\partial T[\Theta(\omega, T)]$ in the high frequency as shown in Fig. 3(b). Therefore, the suppression of near-field heat flux by the magnetic field for $E_F = 0.05 \text{ eV}$ in Fig. 2(b) mainly stems from the decrease of the intraband transition peak of $\Phi(\omega)$ with magnetic field and the blueshift of the first interband transition peak, which results in a lower weight in the heat flux.

For the higher E_F , the low-field bright stripe gets broader and shifts to a higher frequency, and the range where $\Phi(\omega)$ is not affected by the magnetic field becomes wider. As shown in Fig. 3(c), the interband threshold $\hbar\omega \approx 2E_F = 1.0 \text{ eV}$ is out of the frequency range we are interested in and, thus, the spectra of the whole region are

almost identical. The near-zero stripe only appears for a very strong magnetic field and leads to a very slight fluctuation in $h(\omega)$ as shown in Fig. 3(d). Thus, the heat flux for $E_F = 0.5$ eV in Fig. 2(b) is almost independent of the magnetic field.

C. Energy transmission coefficient and dispersion relation

In order to get the physical insights of these phenomena, we now turn to the discussions of energy transfer coefficients and dispersion relations. Although the nondiagonal reflection coefficients r_{sp} and r_{ps} are not equal to zero, their contributions are negligible compared to that of r_{pp} , where r_{mn} is the Fresnel reflection coefficient and m and n represent the polarization states (p or s polarization) of incident waves and reflection waves, respectively. In addition, the contributions of TE (s -polarized) waves and the propagating TM (p -polarized) waves can be neglected in the near field and the contribution of evanescent TM waves plays a dominant role. Therefore, the energy transmission coefficient can be simplified as

$$\mathbf{T}(\omega, k) = \frac{4\text{Im}(r_{pp})\text{Im}(r_{pp})e^{-2kd}}{|1 - r_{pp}r_{pp}e^{-2kd}|^2}, \quad (16)$$

where r_{pp} can be rewritten as

$$r_{pp} = \frac{2Z_0\sigma_L k_z/k_0 + Z_0^2(\sigma_L^2 + \sigma_H^2)}{4 + 2Z_0(k_z/k_0 + k_0/k_z)\sigma_L + Z_0^2(\sigma_L^2 + \sigma_H^2)}. \quad (17)$$

In a perpendicular static magnetic field, graphene supports MPP modes for TM waves and quasi-transverse-electric (QTE) mode for TE waves in the infrared region [42]. Let the denominator of r_{pp} be zero; then we can get the dispersion relation of the MPP mode at the graphene-vacuum interface as follows:

$$\frac{k_z}{k_0} = \frac{-b \pm \sqrt{b^2 - 4a^2}}{2a}, \quad (18)$$

where $a = 2Z_0\sigma_L$, $b = 4 + Z_0^2(\sigma_L^2 + \sigma_H^2)$, and \pm denotes the MPP and QTE modes, respectively. Because $b^2 \gg 4a^2$ and $Z_0^2(\sigma_L^2 + \sigma_H^2) \ll 4$, the dispersion relation can be simplified as

$$k \approx -ik_z = \frac{i2k_0}{Z_0\sigma_L} \quad (19)$$

for MPP modes and $k \approx k_0$ for QTE modes that are negligible to NFRHT. r_{pp} can then be rewritten as

$$r_{pp} = \frac{i\sigma_L}{2k_0/(Z_0k) + i\sigma_L}. \quad (20)$$

It is worth noting that the dispersion relation and the reflection coefficient in the presence of a magnetic field have

the same form as the case in zero field [18], except that the optical conductivity is replaced by the longitudinal magneto-optical conductivity σ_L .

In Fig. 4, we plot the real and imaginary parts of r_{pp} , energy transmission coefficient $\mathbf{T}(\omega, k)$, and energy transfer function $\Phi(\omega)$ as a function of dimensionless frequency $\hbar\omega/E_1$ and wave vector k/k_0 for $B = 10$ T and $E_F = 0.2$ eV. The dashed curves denote the dispersion relation given by Eq. (19). The results show that there are many branches in the real and imaginary parts of r_{pp} due to the contributions of intraband and interband transitions, and the dispersion curves are located at the minimum of $\text{Re}(r_{pp})$ and maximum of $\text{Im}(r_{pp})$. Since MPP modes can only exist when $\text{Im}(\sigma_L) > 0$ as described in Eq. (19), the oscillations of $\text{Im}(\sigma_L)$ around zero at high frequencies give rise to many branches in the dispersion curves, as shown by the white dashed curves in Fig. 4, beginning at the frequency of interband transitions $\hbar\omega = (\sqrt{n} + \sqrt{n+1})E_1$, where $n \geq 2$, and each k corresponds to two ω 's. At low frequency, the interband transitions induced by the thermal effect with energy differences E_1 and $(\sqrt{2} + 1)E_1$ result in weak oscillations in $\text{Im}(\sigma_L)$ but still positive; thus, the dispersion curves connect with each other and also with that due to intraband transition $(\sqrt{2} - 1)E_1$.

When two monolayer graphene sheets get close enough to each other, the MPP modes can be coupled with each

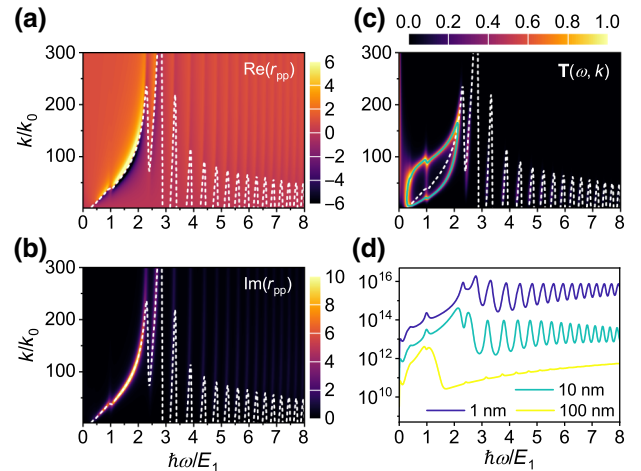


FIG. 4. (a),(b) The real and imaginary parts of the reflection coefficient r_{pp} of graphene and (c) energy transmission coefficient $\mathbf{T}(\omega, k)$ between two monolayer graphene sheets separated by $d = 10$ nm, as a function of dimensionless photon energy $\hbar\omega/E_1$ and dimensionless wave vector k/k_0 for $T = 300$ K, $E_F = 0.2$ eV, and $B = 10$ T. The white dashed curves indicate the dispersion relation of MPP modes in single-layer graphene and the green solid curves in (c) are coupled MPP modes between two monolayer graphene sheets separated by $d = 10$ nm. (d) Energy transfer function $\Phi(\omega)$ as a function of $\hbar\omega/E_1$ at different gap size.

other. The dispersion relation of the coupled MPP modes can be obtained by searching for the poles of $\mathbf{T}(\omega, k)$. Let the denominator of $\mathbf{T}(\omega, k)$ be zero, i.e., $1 - r_{pp}r_{pp}e^{-2kd} = 0$, and we can get two solutions: $r_{pp} = e^{kd}$ (acoustic mode at low frequencies) and $r_{pp} = -e^{kd}$ (optical mode at high frequencies). Then, the dispersion relation of coupled MPP modes can be expressed as

$$\frac{i\sigma_L}{2k_0/(Z_0k) + i\sigma_L} = \pm e^{kd}. \quad (21)$$

When $|r_{pp}| = e^{kd}$, $\mathbf{T}(\omega, k)$ reaches a maximum value of unity. Note that, for MPP modes, we have $\text{Re}(r_{pp}) \ll \text{Im}(r_{pp})$ [see Figs. 4(a) and 4(b)]; therefore, the energy transmission coefficient can be further simplified as $\mathbf{T}(\omega, k) = 4/(\zeta + 1/\zeta + 2)$, where $\zeta = [\text{Im}(r_{pp})e^{-kd}]^2$.

The low-frequency MPP modes between two graphene sheets are coupled with each other at $d = 10$ nm and the dispersion relation splits into two branches: an acoustic mode and optical mode, corresponding to the maximum value $\mathbf{T}(\omega, k) = 1.0$ and converging at high k/k_0 , as shown by the green curves in Fig. 4(c). There are three parallel bright stripes at $\hbar\omega/E_1 \approx 0.4, 1.0, \text{ and } 2.1$, corresponding to the three peaks at the same frequencies in the green curve in Fig. 4(d).

Meanwhile, at high frequencies, the oscillatory attenuations of the real and imaginary parts of the conductivity result in the reduction of the local maximum value of the reflection coefficient, such that $|r_{pp}| < e^{-kd}$, failing to satisfy Eq. (21), and the MPP modes cannot be coupled. Since we have $\zeta < 1$, $\mathbf{T}(\omega, k)$ monotonically increases with ζ . Therefore, in Fig. 4(c), a series of parallel bright stripes appears in the vicinity of the dispersion curves, because the high-frequency uncoupled MPP modes give rise to large local density of states (LDOS), which are proportional to $\text{Im}(r_{pp})e^{-kd}$ [1]. However, the uncoupled MPP does not have an asymptote parallel to k to produce a strong resonance and, thus, $|r_{pp}|$ has a limited value that cannot compensate for the exponential decay factor e^{-2kd} in ζ . Therefore, the values of the high-frequency bright stripes in $\mathbf{T}(\omega, k)$ are less than 1.0 and decay significantly with k and d , resulting in a smaller contributing k . Thus in Fig. 4(d) we can see that these parallel bright stripes originating oscillating peaks in $\Phi(\omega)$, whose frequencies are close but not exactly equal to interband transition with energy gaps $\hbar\omega \approx (\sqrt{n} + \sqrt{n+1})E_1$ ($n \geq 1$) because they are also dependent of the gap size, shifting slightly with d , and whose values are much less than that caused by coupled MPP modes and decrease with frequency, because $\text{Im}(r_{pp})$ has smaller values of at higher frequencies, the MPP modes are more easily decoupled as d increases, and the high-frequency peaks in $\Phi(\omega)$ have faster decay rates. In turn, the coupling states of the high-frequency MPP modes can be changed by reducing the gap size or enhancing the magnetic field. There is an another

peak at near-zero frequency, induced by neither the MPP mode [$\text{Im}(\sigma_L) < 0$] nor the QTE mode ($k \gg k_0$). The main reason for this peak is that $\text{Im}(r_{pp})$ has a local maximum at this frequency, thus causing a large LDOS.

To further understand the effect of magnetic fields on the near-field thermal radiation of graphene at different Fermi energies, in Fig. 5, we plot the contours of $\mathbf{T}(\omega, k)$ as a function of k/k_0 and ω at $B = 10$ T ($E_1 \approx 0.11$ eV) for Fermi energies of 0.05, 0.2, and 0.5 eV. The left three panels in Fig. 5 are $\mathbf{T}(\omega, k)$ in the presence of a magnetic field, where the dashed curves represent the dispersion relation of coupled MPP, and the right three panels represent the zero-field $\mathbf{T}(\omega, k)$ for different values of E_F .

As one can see, $\mathbf{T}(\omega, k)$ values for the low Fermi energy ($E_F = 0.05$ eV) are significantly modified by the strong magnetic field compared to that in zero field. $\mathbf{T}(\omega, k)$ values are greatly enhanced in zero field due to the coupled surface plasmons, showing two bright stripes, and most of the energies are concentrated in the low-frequency region. When a strong magnetic field is applied, the stripes split into several stripes distributed through the whole frequency region, including the bright stripes with values near unity arising from the coupled MPP modes and the series of parallel stripes due to the large LDOS of uncoupled MPP at high frequencies. The values of high-frequency

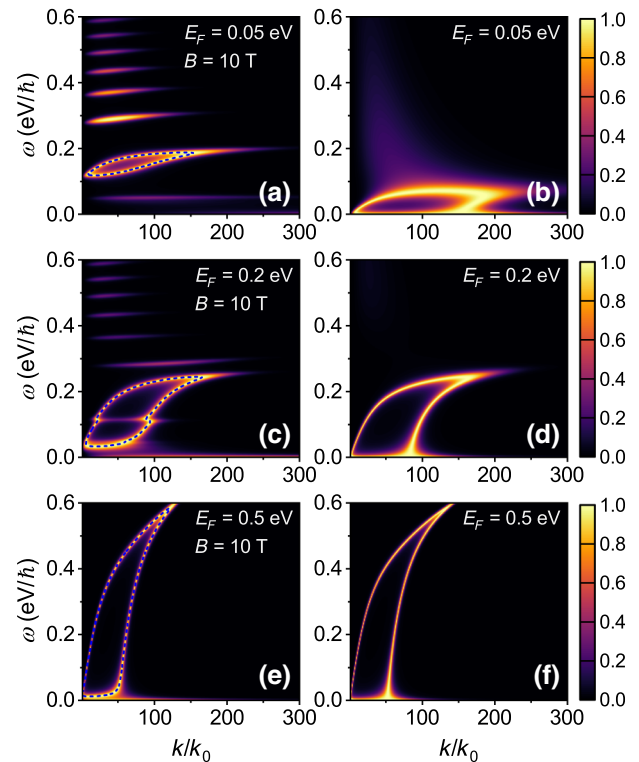


FIG. 5. Contour plots of the energy transmission coefficient as a function of dimensionless k/k_0 and angular frequency ω for $E_F = 0.05$ eV, $E_F = 0.2$ eV, and $E_F = 0.5$ eV, with $B = 10$ T (left three panels) and zero field (right three panels).

stripes can be comparable to that due to coupled MPP and they decrease with frequency. When $E_F = 0.2$ eV, the coupled MPP modes produce a mild fluctuation compared with that due to the zero-field SPP, while high-frequency uncoupled MPP modes give rise to significantly lower values of $\mathbf{T}(\omega, k)$ than those of the coupled MPP. For $E_F = 0.5$ eV, the $\mathbf{T}(\omega, k)$ in a magnetic field and in zero field are approximately the same and the uncoupled MPP modes shift to higher frequencies (not shown), which have a negligible effect on near-field heat flux. Therefore, the heat flux for high Fermi energy is almost constant in different magnetic fields.

D. Near-field radiative heat transfer coefficient vs B and E_F

In Fig. 6, we plot the RHTC and the ratio of RHTC in a magnetic field to zero field as a function of E_F and B . The other parameters are taken as $d = 10$ nm and $T = 300$ K. The dashed curve denotes $h(0, E_F)/h(B, E_F) = 1.0$ or TMR = 0. The results demonstrate that the influence of a magnetic field on the radiative heat flux is mainly concentrated on the low Fermi energy. We observe the reduction of the near-field radiative heat flux at low Fermi energies, especially for $E_F < 0.1$ eV, leading to a positive thermal magnetoresistance increasing with the magnetic field, because the first Landau level E_1 increases with magnetic field and low-frequency intraband transitions are partially blocked at room temperature. Thus, spectral peaks in $\Phi(\omega)$ shift to high frequencies with lower weights in heat flux. When $E_F > 0.3$ eV, the magnetic field, even up to 20 T, can hardly cause large fluctuations in the heat flux. Because at high Fermi energies, low-frequency interband transitions are blocked and high-frequency ones whose contributions are negligible decay exponentially at room temperature, the intraband transition dominates, but its contribution is hardly affected by the magnetic field. It is shown in Fig. 6(a) that for a given magnetic field,

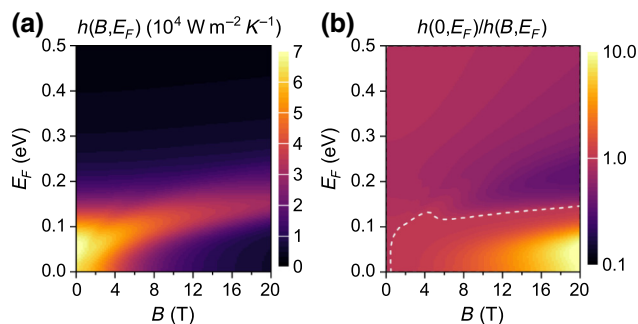


FIG. 6. (a) RHT between two graphene sheets as a function of E_F and B . (b) Ratio of RHT in zero field to that in the presence of a magnetic field for the same Fermi energy. The dashed curve denotes $h(0, E_F)/h(B, E_F) = 1.0$. The temperature and the gap size in (a) and (b) are $T = 300$ K and $d = 10$ nm, respectively.

there exists an optimal Fermi energy $E_{F \max}$ such that the heat flux reaches the maximum h_{\max} . h_{\max} decreases monotonically with the field, corresponding to a higher $E_{F \max}$, for example, $h_{\max} \approx 7.0 \times 10^4$ W m $^{-2}$ K $^{-1}$ at $E_{F \max} \approx 0.06$ eV in zero field, while $h_{\max} \approx 3.0 \times 10^4$ W m $^{-2}$ K $^{-1}$ at $E_{F \max} \approx 0.15$ eV for $B = 20$ T, producing a reduction of over 50%. Therefore, the heat flux decreases with magnetic field at $E_F \geq E_{F \max}$, as shown in Fig. 6(b); $h(0, E_F)/h(B, E_F)$ is minimized in the vicinity of $E_{F \max}$, less than 1.0; and TMR is negative and decreases with magnetic field, as low as -55% at $B = 20$ T. In contrast, for $E_F < E_{F \max}$, RHTC decreases with magnetic field, resulting in an increasing thermal magnetoresistance. Thus, $h(0, E_F)/h(B, E_F) > 1.0$ and TMR is positive.

E. The effect of temperature

In addition to the Fermi energy, magnetic field, and gap size, the temperature of graphene also affects the NFRHT in a magnetic field, not only by modifying the average photon energy $\Theta(\omega, T)$, shifting more energy of thermal radiation to high frequencies (corresponding to Wien's displacement law in the far field), but also by changing the magneto-optical conductivity by the term of the Fermi-Dirac distribution difference $n_F(E_n) - n_F(E_m)$ in Eq. (11). The thermal effect can broaden the range of the interband transition of graphene at a high Fermi energy, so that the interband transition can also occur at a frequency of several $k_B T$ below the threshold; it also increases the probability of intraband transitions of graphene at a low Fermi energy. Therefore, high temperatures can give rise to oscillations in the radiative spectrum of graphene at high Fermi energies in the magnetic field. In Fig. 7(a), we plot the transfer function $\Phi(\omega)$ as a function of the dimensionless frequency $\hbar\omega/E_1$ for $E_F = 0.5$ eV at different temperatures, which excludes the effect of temperature on $\Theta(\omega, T)$. We find that at higher temperatures, the oscillations and a series of peaks can be observed at lower frequencies. The curves at low temperatures significantly deviate from the zero-field spectrum at frequencies where the oscillation begins, as shown by the dark blue and light blue curves, while high-temperature spectrums almost oscillate around the zero-field value.

Although for a high Fermi energy the spectrum of graphene at high temperature is more susceptible to magnetic field than that at low temperature, the heat flux does not change significantly, which means that the magnetic field significantly changes the spectral energy distribution of NFRHT, but the heat flux remains approximately constant. As shown in Figs. 7(b) and 7(c), the maximum values of RHTC and the ratio are shifted to high E_F , but the modulation of magnetic field is weaker than that at room temperature, as shown in Fig. 6, especially for low Fermi energies, and even in a magnetic field up to 20 T, the relative change of heat flux does not exceed 30%. We speculate

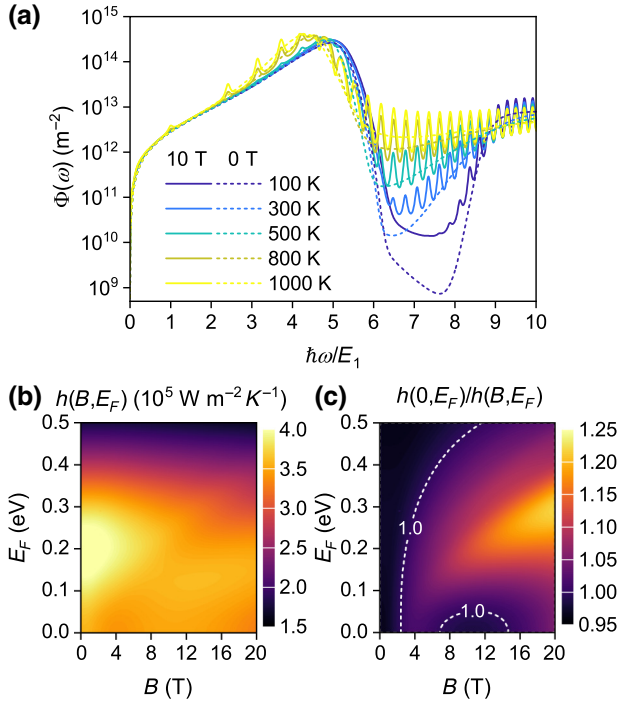


FIG. 7. (a) Temperature-dependent energy transfer function $\Phi(\omega)$ between two graphene sheets as a function of the dimensionless $\hbar\omega/E_1$ for $E_F = 0.5$ eV. The solid and dashed curves represent $B = 10$ T and $B = 0$ T, respectively. Since there is no Landau level in zero field, for convenience, E_1 in the horizontal axis is taken the same as that at $B = 10$ T, and the interband threshold is $\hbar\omega/E_1 = \sqrt{N_F + 1} + \sqrt{N_F} \approx 8.6$. (b),(c) RHTC and ratio of zero-field RHTC to non-zero-field RHTC between two graphene sheets at $T = 1000$ K, separated by a vacuum gap of 10 nm as a function of E_F and B .

that the thermal effect gives rise to high transition probabilities and fewer transitions are blocked, and although the high-temperature spectrum oscillates more strongly, it is more confined to the zero-field spectrum. Therefore, the heat flux by the integral over the whole spectrum is more approximate to that in zero field.

F. Discussion

In a magnetic field, because of the intraband and interband transitions between various Landau levels and excited magneto-plasmons in graphene, a series of oscillating peaks is observed in the near-field radiative spectrum, and the magnetic field can realize strong active control of near-field heat flux, giant thermal magnetoresistance, and negative thermal magnetoresistance. The requirement for strong external magnetic fields, especially for graphene with a high Fermi energy, may limit its practical applications, but nevertheless there are still some promising applications, such as magnetic sensing and noncontact active control or thermal switching of near-field heat flux through

a strong magnetic field, that can be used for thermal management in micro and nano systems. The pulsed magnetic field can be used to realize the near-field radiative thermal signals, which may have some applications in thermal circuits and information processing. In addition, we note that graphene can achieve strong pseudomagnetic fields through strain [49,50], even up to 300 T [51], which means that it is possible to achieve the effects discussed above, or even stronger, by applying tiny strains to graphene. Moreover, we note that some other materials, such as two-dimensional black phosphorus [52] and topological materials [53,54], have similar magneto-optical phenomena, and we expect that their near-field thermal radiation may have similar results, but the required magnetic field may be smaller.

V. CONCLUSIONS

In summary, we investigate the near-field radiative energy exchange between two single-layer graphene sheets in the presence of a perpendicular magnetic field. It is found that the coupling of the excited MPP modes of graphene in the near field greatly enhances the radiative heat transfer, which is several orders of magnitude higher than that of the black body. Compared with the SP in zero magnetic field, MPP splits into multiple branches. Because of the intraband and interband transitions at various Landau levels, a series of peaks appears in the near-field radiative spectral heat flux, giving rise to SDH-like oscillations around the zero-field spectrum. Moreover, we demonstrate that a magnetic field can achieve strong active control of the near-field radiative heat transfer. At room temperature, the near-field heat transfer coefficients of graphene at lower Fermi energies are strongly suppressed with the increase of the magnetic field, showing giant thermal magnetoresistances. The maximum TMR can reach 50 at $B = 20$ T. In contrast, for graphene at high Fermi energies, the magnetic field has a trivial effect on the heat flux, producing negative thermal magnetoresistances, which is a thermal analogy of the negative thermal magnetoresistance for some material (such as ferromagnetic materials and topological materials) in electronics. In the far field, the net heat flux is enhanced by the magnetic field, for graphene at both high and low E_F , showing negative thermal magnetoresistances and TMR as low as -90% . At high temperature, the magnetic field significantly changes the spectral energy distribution of NFRHT, but the heat flux remains approximately constant. We expect that our demonstration may find some potential applications in noncontact thermal management.

ACKNOWLEDGMENTS

This work was supported by the National Science Foundation of China (Grants No. 51876004 and No. 51406006).

-
- [1] J. B. Pendry, Radiative exchange of heat between nanostructures, *J. Phys. Condens. Matter* **11**, 6621 (1999).
- [2] K. Joulain, J.-P. Mulet, F. Marquier, R. Carminati, and J.-J. Greffet, Surface electromagnetic waves thermally excited: Radiative heat transfer, coherence properties and Casimir forces revisited in the near field, *Surf. Sci. Rep.* **57**, 59 (2005).
- [3] J. Shen, X. Liu, and Y. Xuan, Near-Field Thermal Radiation between Nanostructures of Natural Anisotropic Material, *Phys. Rev. Appl.* **10**, 034029 (2018).
- [4] A. Narayanaswamy and G. Chen, Surface modes for near field thermophotovoltaics, *Appl. Phys. Lett.* **82**, 3544 (2003).
- [5] B. Zhao, K. Chen, S. Buddhiraju, G. Bhatt, M. Lipson, and S. Fan, High-performance near-field thermophotovoltaics for waste heat recovery, *Nano Energy* **41**, 344 (2017).
- [6] R. St-Gelais, G. R. Bhatt, L. Zhu, S. Fan, and M. Lipson, Hot carrier-based near-field thermophotovoltaic energy conversion, *ACS Nano* **11**, 3001 (2017).
- [7] A. Fiorino, L. Zhu, D. Thompson, R. Mittapally, P. Reddy, and E. Meyhofer, Nanogap near-field thermophotovoltaics, *Nat. Nanotechnol.* **13**, 806 (2018).
- [8] Y. De Wilde, F. Formanek, R. Carminati, B. Gralak, P.-A. Lemoine, K. Joulain, J.-P. Mulet, Y. Chen, and J.-J. Greffet, Thermal radiation scanning tunnelling microscopy, *Nature* **444**, 740 (2006).
- [9] W. A. Challener, C. Peng, A. V. Itagi, D. Karns, W. Peng, Y. Peng, X. Yang, X. Zhu, N. J. Gokemeijer, Y. T. Hsia, G. Ju, R. E. Rottmayer, M. A. Seigler, and E. C. Gage, Heat-assisted magnetic recording by a near-field transducer with efficient optical energy transfer, *Nat. Photonics* **3**, 220 (2009).
- [10] K. Chen, P. Santhanam, S. Sandhu, L. Zhu, and S. Fan, Heat-flux control and solid-state cooling by regulating chemical potential of photons in near-field electromagnetic heat transfer, *Phys. Rev. B* **91**, 134301 (2015).
- [11] K. Chen, P. Santhanam, and S. Fan, Near-Field Enhanced Negative Luminescent Refrigeration, *Phys. Rev. Appl.* **6**, 024014 (2016).
- [12] X. Liu and Z. M. Zhang, High-performance electroluminescent refrigeration enabled by photon tunneling, *Nano Energy* **26**, 353 (2016).
- [13] C. R. Otey, W. T. Lau, and S. Fan, Thermal Rectification Through Vacuum, *Phys. Rev. Lett.* **104**, 154301 (2010).
- [14] A. Fiorino, D. Thompson, L. Zhu, R. Mittapally, S.-A. Biehs, O. Bezencenet, N. El-Bondry, S. Bansropun, P. Ben-Abdallah, E. Meyhofer, and P. Reddy, A thermal diode based on nanoscale thermal radiation, *ACS Nano* **12**, 5774 (2018).
- [15] P. Ben-Abdallah and S.-A. Biehs, Near-Field Thermal Transistor, *Phys. Rev. Lett.* **112**, 044301 (2014).
- [16] T. Low and P. Avouris, Graphene plasmonics for terahertz to mid-infrared applications, *ACS Nano* **8**, 1086 (2014).
- [17] O. D. Miller, O. Ilic, T. Christensen, M. T. H. Reid, H. A. Atwater, J. D. Joannopoulos, M. Soljačić, and S. G. Johnson, Limits to the optical response of graphene and two-dimensional materials, *Nano Lett.* **17**, 5408 (2017).
- [18] O. Ilic, M. Jablan, J. D. Joannopoulos, I. Celanovic, H. Buljan, and M. Soljačić, Near-field thermal radiation transfer controlled by plasmons in graphene, *Phys. Rev. B* **85**, 155422 (2012).
- [19] J.-H. Jiang and J.-S. Wang, Caroli formalism in near-field heat transfer between parallel graphene sheets, *Phys. Rev. B* **96**, 155437 (2017).
- [20] F. V. Ramirez and A. J. H. McGaughey, Plasmonic thermal transport in graphene nanodisk waveguides, *Phys. Rev. B* **96**, 165428 (2017).
- [21] R. Yu, A. Manjavacas, and F. J. García de Abajo, Ultrafast radiative heat transfer, *Nat. Commun.* **8**, 2 (2017).
- [22] O. Ilic, N. H. Thomas, T. Christensen, M. C. Sherrott, M. Soljačić, A. J. Minnich, O. D. Miller, and H. A. Atwater, Active radiative thermal switching with graphene plasmon resonators, *ACS Nano* **12**, 2474 (2018).
- [23] A. I. Volokitin and B. N. J. Persson, Near-field radiative heat transfer between closely spaced graphene and amorphous SiO₂, *Phys. Rev. B* **83**, 241407 (2011).
- [24] R. Messina, J.-P. Hugonin, J.-J. Greffet, F. Marquier, Y. De Wilde, A. Belarouci, L. Frechette, Y. Cordier, and P. Ben-Abdallah, Tuning the electromagnetic local density of states in graphene-covered systems via strong coupling with graphene plasmons, *Phys. Rev. B* **87**, 085421 (2013).
- [25] P. J. Van Zwol, S. Thiele, C. Berger, W. A. De Heer, and J. Chevrier, Nanoscale Radiative Heat Flow Due to Surface Plasmons in Graphene and Doped Silicon, *Phys. Rev. Lett.* **109**, 264301 (2012).
- [26] J. Yang, W. Du, Y. Su, Y. Fu, S. Gong, S. He, and Y. Ma, Observing of the super-Planckian near-field thermal radiation between graphene sheets, *Nat. Commun.* **9**, 4033 (2018).
- [27] B. Zhao and Z. M. Zhang, Enhanced photon tunneling by surface plasmon-Phonon polaritons in graphene/hBN heterostructures, *J. Heat Transf.* **139**, 022701 (2016).
- [28] R. Messina and P. Ben-Abdallah, Graphene-based photovoltaic cells for near-field thermal energy conversion, *Sci. Rep.* **3**, 1383 (2013).
- [29] V. B. Svetovoy and G. Palasantzas, Graphene-on-Silicon Near-Field Thermophotovoltaic Cell, *Phys. Rev. Appl.* **2**, 034006 (2014).
- [30] E. Moncada-Villa, V. Fernández-Hurtado, F. J. García-Vidal, A. García-Martín, and J. C. Cuevas, Magnetic field control of near-field radiative heat transfer and the realization of highly tunable hyperbolic thermal emitters, *Phys. Rev. B* **92**, 125418 (2015).
- [31] L. Zhu and S. Fan, Persistent Directional Current at Equilibrium in Nonreciprocal Many-Body Near Field Electromagnetic Heat Transfer, *Phys. Rev. Lett.* **117**, 134303 (2016).
- [32] P. Ben-Abdallah, Photon Thermal Hall Effect, *Phys. Rev. Lett.* **116**, 084301 (2016).
- [33] I. Latella and P. Ben-Abdallah, Giant Thermal Magnetoresistance in Plasmonic Structures, *Phys. Rev. Lett.* **118**, 173902 (2017).
- [34] R. M. Abraham Ekeroth, P. Ben-Abdallah, J. C. Cuevas, and A. García-Martín, Anisotropic thermal magnetoresistance for an active control of radiative heat transfer, *ACS Photonics* **5**, 705 (2018).

- [35] I. Crassee, J. Levallois, A. L. Walter, M. Ostler, A. Bostwick, E. Rotenberg, T. Seyller, D. van der Marel, and A. B. Kuzmenko, Giant Faraday rotation in single- and multilayer graphene, *Nat. Phys.* **7**, 48 (2011).
- [36] R. Shimano, G. Yumoto, J. Y. Yoo, R. Matsunaga, S. Tanabe, H. Hibino, T. Morimoto, and H. Aoki, Quantum Faraday and Kerr rotations in graphene, *Nat. Commun.* **4**, 1841 (2013).
- [37] T. Morimoto, Y. Hatsugai, and H. Aoki, Optical Hall Conductivity in Ordinary and Graphene Quantum Hall Systems, *Phys. Rev. Lett.* **103**, 116803 (2009).
- [38] M. L. Sadowski, G. Martinez, M. Potemski, C. Berger, and W. A. de Heer, Landau Level Spectroscopy of Ultrathin Graphite Layers, *Phys. Rev. Lett.* **97**, 266405 (2006).
- [39] Z. Jiang, E. A. Henriksen, L. C. Tung, Y.-J. Wang, M. E. Schwartz, M. Y. Han, P. Kim, and H. L. Stormer, Infrared Spectroscopy of Landau Levels of Graphene, *Phys. Rev. Lett.* **98**, 197403 (2007).
- [40] K. W. Chiu and J. J. Quinn, Plasma oscillations of a two-dimensional electron gas in a strong magnetic field, *Phys. Rev. B* **9**, 4724 (1974).
- [41] O. L. Berman, G. Gumbs, and Y. E. Lozovik, Magneto-plasmons in layered graphene structures, *Phys. Rev. B* **78**, 085401 (2008).
- [42] A. Ferreira, N. M. R. Peres, and A. H. Castro Neto, Confined magneto-optical waves in graphene, *Phys. Rev. B* **85**, 205426 (2012).
- [43] X. Dai, Z. Z. Du, and H.-Z. Lu, Negative Magnetoresistance without Chiral Anomaly in Topological Insulators, *Phys. Rev. Lett.* **119**, 166601 (2017).
- [44] S.-A. Biehs, P. Ben-Abdallah, F. S. S. Rosa, K. Joulain, and J.-J. Greffet, Nanoscale heat flux between nanoporous materials, *Opt. Express* **19**, A1088 (2011).
- [45] J. Shen, S. Guo, X. Liu, B. Liu, W. Wu, and H. He, Super-Planckian thermal radiation enabled by coupled quasi-elliptic 2D black phosphorus plasmons, *Appl. Therm. Eng.* **144**, 403 (2018).
- [46] L. A. Falkovsky, Optical properties of graphene, *J. Phys. Conf. Ser.* **129**, 012004 (2008).
- [47] A. Ferreira, J. Viana-Gomes, Y. V. Bludov, V. Pereira, N. M. R. Peres, and A. H. Castro Neto, Faraday effect in graphene enclosed in an optical cavity and the equation of motion method for the study of magneto-optical transport in solids, *Phys. Rev. B* **84**, 235410 (2011).
- [48] V. P. Gusynin, S. G. Sharapov, and J. P. Carbotte, Magneto-optical conductivity in graphene, *J. Phys. Condens. Matter* **19**, 1 (2007).
- [49] F. Guinea, M. I. Katsnelson, and A. K. Geim, Energy gaps and a zero-field quantum hall effect in graphene by strain engineering, *Nat. Phys.* **6**, 30 (2010).
- [50] D.-B. Zhang, G. Seifert, and K. Chang, Strain-Induced Pseudomagnetic Fields in Twisted Graphene Nanoribbons, *Phys. Rev. Lett.* **112**, 096805 (2014).
- [51] N. Levy, S. A. Burke, K. L. Meaker, M. Panlasigui, A. Zettl, F. Guinea, A. H. C. Neto, and M. F. Crommie, Strain-Induced Pseudo-Magnetic Fields Greater Than 300 Tesla in Graphene Nanobubbles, *Science (80-.)* **329**, 544 (2010).
- [52] M. Tahir, P. Vasilopoulos, and F. M. Peeters, Magneto-optical transport properties of monolayer phosphorene, *Phys. Rev. B* **92**, 045420 (2015).
- [53] Z. Li and J. P. Carbotte, Magneto-optical conductivity in a topological insulator, *Phys. Rev. B* **88**, 045414 (2013).
- [54] K. Rahim, A. Ullah, M. Tahir, and K. Sabeeh, Magneto-optical properties of topological insulator thin films with broken inversion symmetry, *J. Phys. Condens. Matter* **29**, 425304 (2017).